

Optimal INS/GNSS Coupling for Autonomous Car Positioning Integrity

Çağatay Tanıl, *Amazon Prime Air*,
Samer Khanafseh, *Illinois Institute of Technology*,
Mathieu Joerger, *Virginia Tech*,
Birendra Kujur, *Illinois Institute of Technology*,
Brett Kruger, Lance de Groot, *Hexagon Positioning Intelligence*,
Boris Pervan, *Illinois Institute of Technology*

BIOGRAPHIES

Dr. Çağatay Tanıl received his B.S. and M.S. in Mechanical Engineering from Middle East Technical University, in 2006 and 2009, respectively; and Ph.D. in Aerospace Engineering from Illinois Institute of Technology (IIT) in 2016. His doctoral work, detecting GNSS spoofing attacks using INS coupling, was awarded by the 2017 Institute of Navigation (ION) Bradford W. Parkinson Award for excellence in global navigation satellite systems. With more than 13 years of guidance, navigation, and control experience, Dr. Tanıl fulfilled many research and development roles. From 2006 to 2013, he worked at leading defense and aerospace companies in Turkey, including Roketsan Missiles Industries, Turkish Aerospace Industries (TAI), and Defense Industries Research and Development Institute (Tubitak-SAGE). From 2016 to 2019, Dr. Tanıl worked at IIT as a Senior Research Associate, and at TruNav LLC as a research scientist, where he developed ARAIM-based satellite fault detection and exclusion algorithms, and autonomous car position integrity. Dr. Tanıl is currently a Navigation Research Scientist at Amazon Prime Air, working on drone navigation and safety.

Dr. Samer Khanafseh is currently a research assistant professor at Illinois Institute of Technology (IIT), Chicago. He received his MSc and PhD degrees in Aerospace Engineering from IIT in 2003 and 2008, respectively. Dr. Khanafseh has been involved in several aviation applications such as Autonomous Airborne Refueling (AAR) of unmanned air vehicles, autonomous shipboard landing for NUCAS and JPALS programs and Ground Based Augmentation System (GBAS). His research interests are focused on high accuracy and high integrity navigation algorithms, cycle ambiguity resolution, high integrity applications, fault monitoring and robust estimation techniques. He was the recipient of the 2011 Institute of Navigation Early Achievement Award for his outstanding contributions to the integrity of carrier phase navigation systems.

Dr. Mathieu Joerger obtained a Master in Mechatronics from the National Institute of Applied Sciences in Strasbourg, France, in 2002. He earned a M.S. in 2002 and a Ph.D. in 2009 in Mechanical and Aerospace Engineering at IIT in Chicago. He is the 2009 recipient of the Institute of Navigation (ION) Bradford Parkinson award, and the 2014 recipient of the (ION) Early Achievement Award. He is also an Associate Editor of Navigation for the Institute of Electrical and Electronics Engineers (IEEE) Transactions on Aerospace and Electronic Systems. Dr. Joerger is currently assistant professor at Virginia Tech, in Blacksburg, VA, working on multi-sensor integration for safe navigation and collision warning of automated driving systems (ADS). He is a member of the E.U./U.S. Advanced RAIM (ARAIM) Working Group C.

Birendra Kujur is a PhD candidate in Navigation Lab at Illinois Institute of Technology. He received his Bachelor of Science in Mechanical Engineering from Purdue University in 2014. His research interests include Multi-Sensor Navigation systems and Navigation Integrity Monitoring.

Bret Kruger is a Software engineer working within PIs Safety Critical Systems group. With his background in INS, he leads the development of ASIL rated inertial software targeting autonomous driving applications. Brett graduated with a MAsc in Electrical engineering from the University of Toronto in 2012.

Lance de Groot holds a B.Sc. and M.Sc. in Geomatics Engineering from the University of Calgary. He joined Hexagon Positioning Intelligence (PI) in 2008 and has worked on ground reference receivers for SBAS networks,

high precision positioning and relative alignment algorithms for commercial applications, and safety critical software for autonomous applications. He is currently a member of PIs Safety Critical Systems group.

Dr. Boris Pervan is a Professor of Mechanical and Aerospace Engineering at IIT, where he conducts research on advanced navigation systems. Prior to joining the faculty at IIT, he was a spacecraft mission analyst at Hughes Aircraft Company (now Boeing) and a postdoctoral research associate at Stanford University. Prof. Pervan received his B.S. from the University of Notre Dame, M.S. from the California Institute of Technology, and Ph.D. from Stanford University. He is an Associate Fellow of the AIAA, a Fellow of the Institute of Navigation (ION), and Editor-in-Chief of the ION journal NAVIGATION. He was the recipient of the IIT Sigma Xi Excellence in University Research Award (2011, 2002), Ralph Barnett Mechanical and Aerospace Dept. Outstanding Teaching Award (2009, 2002), Mechanical and Aerospace Dept. Excellence in Research Award (2007), University Excellence in Teaching Award (2005), IEEE Aerospace and Electronic Systems Society M. Barry Carlton Award (1999), RTCA William E. Jackson Award (1996), Guggenheim Fellowship (Caltech 1987), and Albert J. Zahm Prize in Aeronautics (Notre Dame 1986).

ABSTRACT

Safe positioning is a critical capability for automated driving systems (ADAS). This paper describes optimal integration and filtering schemes of Inertial Measurement Units (IMU) and Global Navigation Satellite Systems (GNSS) measurements to improve and quantify positioning integrity in urban canyons with poor satellite signals. For a predefined integrity requirement, minimum achievable protection levels are quantified for realistic urban navigation scenarios.

I. INTRODUCTION

With the emergence of automated driving system (ADS) technology, the era of autonomous vehicles is fast approaching [1]. Unfortunately, it is still unclear whether driverless cars will be safe once they are released on the mass market. A comparison of ADS with GNSS-based aircraft autopilot systems provides valuable insights [2]. However, aviation safety methods cannot directly be transferred to GNSS-based ground applications. The reason is that aircraft integrity monitoring algorithms leverage satellite redundancy under open sky conditions, which is not available in urban environments due to buildings and trees causing poor sky visibility. This paper describes optimal integration and filtering schemes of Inertial Measurement Units (IMU) and Global Navigation Satellite Systems (GNSS) to improve and, more importantly, quantify positioning integrity in urban canyons.

Highly automated vehicles rely on two key operational capabilities: enabling timely hazard sense and avoid maneuvers in a changing environment, and keeping the vehicle moving along a desired trajectory. To achieve the former, vision/radar/LiDAR based approaches can be used for the detection of road obstructions, lane markings, and other road users. The latter, which this work addresses, requires a navigation system having a sub-decimeter level accuracy. This can be achieved using augmented GNSS, for example using Precise Point Positioning (PPP) [3] or Real Time Kinematic (RTK). These techniques rely on correction data provided by a reference station or network. Unfortunately, GNSS signals can be degraded in urban environments; therefore, even when corrections are available, they do not effectively guarantee that protection levels will be low enough to enable safe driving.

In recent years, different solutions have been proposed in terms of integrity monitoring in urban environments [4]. These include hybridization of GNSS with other sensors such as inertial sensors [5] and vision sensors with map matching techniques [6], and measurement rejection-based Random Sample Consensus (RANSAC) methods [7]. In this work, we focus on integration of GNSS and INS measurements to ensure integrity because inertial sensors are already incorporated with GNSS receivers in most automotive navigation systems, therefore additional hardware or software is not required.

INS and GNSS measurements can be integrated in different schemes (uncoupled, loosely-, tightly-, or ultra-tightly coupled) through a Kalman filter (KF) for estimation and multiple-hypothesis solution separation (MHSS) for detection [8]. In MHSS, under a given fault hypothesis, the detection test statistic is the difference between the full-set solution using all sensor measurements and the subset fault-free solution that excludes all observations associated with a hypothesized fault. Therefore, in MHSS, multiple estimators are needed to compute the full-set and subset solutions. The number of these estimators corresponds to the number of hypotheses, which can reach tens

to hundreds when monitoring against single and dual-satellite orbit and clock faults in multi-constellation GNSS [9]. In time-sequential implementations, this requires that banks of KFs be processed. Recent work [10] proposed a method to reduce computation complexity of KF-based MHSS using suboptimal filters. In our previous work [11], we derived a new time-sequential integrity monitoring technique using the innovation sequence of a single KF. Its performance against worst-case satellite failures was also verified on a tightly coupled INS/GNSS system for aircraft en route and approach operations.

In this work, we evaluate and compare the performance of MHSS-based versus innovation sequence-based integrity monitors for automotive INS/GNSS systems, considering worst-case single-satellite faults. Unlike baseline Receiver Autonomous Integrity Monitoring (RAIM) approaches relying on GNSS redundancy, we here investigate scenarios where there is no satellite redundancy throughout most of the operation, i.e., where the number of satellites is equal or lower than four, which is often the case in urban canyons. One of the challenges in such rapidly changing environments is multipath modeling, especially the characterization of local effects, which can impact integrity monitoring. To realistically model multipath effects, we use stochastic models obtained in our prior work [12]. These values were obtained from a data set collected on a vehicle traveling in an urban canyon and on a highway with overpasses and road signs. Furthermore, to leverage ground vehicle dynamic constraints, including holonomic (no displacement perpendicular to road surface) and non-holonomic (no lateral sliding) constraints, a novel reduced-order INS mechanization is derived, and is incorporated in both the MHSS-based and innovation sequence-based monitors. Covariance analyses show that even in the absence of satellite redundancy, the use of dynamic constraints with a low cost automotive-grade inertial system can provide the means to ensure tight protection levels over time-periods long enough to maneuver out of hazardous situations.

GNSS-based urban navigation is impacted by frequent satellite blockages caused by buildings and other obstructions in the surrounding environment. In solution separation-based integrity monitoring, where there is a Kalman filter for each satellite failure mode, this may require re-initialization and/or termination of some of the subset filters. The re-initialization avoids carrying the effect of potential undetected faults (on the satellites previously in view) on inertial bias states, which eliminates the integrity risk associated with the blocked satellites. However, reinitialization causes a temporary period of poor detection capability until the filters converge again. This paper proposes a novel sub-filter handling using "fading filters" that temporarily monitor prior faults associated with blocked satellites. The proposed approach does not require filter re-initialization therefore eliminates INS memory loss and attenuates potential jumps in protection levels due to weakened geometry.

For a predefined integrity risk requirement, this paper describes optimal integration and filtering techniques for INS/GNSS and identifies the most effective fault monitoring method to achieve minimum protection levels under poor satellite geometries. Therefore, the methodology here is foundational to determine and then meet integrity specifications in urban navigation applications. For example, under ARAIM assumptions on prior satellite fault probabilities and integrity risk requirement, the paper shows that sub-meter level protection levels are achievable using low-cost IMUs tightly-coupled to differential GNSS when four satellites are visible. With three or fewer satellites, depending on the duration of operation, INS-only coasting may provide tighter protection levels than tightly coupled INS/GNSS. It should be noted that the results of this work are specific to automotive applications, but the methods introduced here are also applicable to other applications using INS/GNSS for navigation.

II. REVIEW OF KALMAN FILTER INTEGRITY MONITORS

A. Innovation Sequence Monitor

A nominal INS/GNSS tightly-coupled mechanization can be done through a Kalman filter [5]. The Kalman filter time update is

$$\bar{\mathbf{x}}_k = \Phi \hat{\mathbf{x}}_{k-1} + \Gamma \tilde{\mathbf{u}}_{k-1} \quad (1)$$

where Φ is the state transition matrix of the process model, $\tilde{\mathbf{u}}_k$ is the IMU measurement vector, Γ is the IMU input coefficient matrix, and $\bar{\mathbf{x}}_k$ ($m \times 1$) is the a priori estimate of \mathbf{x} at time epoch k . In this work, \mathbf{x} is a vector containing position, velocity, attitude, and systematic IMU and GNSS measurement biases.

The measurement update gives the a posteriori estimate $\hat{\mathbf{x}}_k$ as

$$\hat{\mathbf{x}}_k = \bar{\mathbf{x}}_k + \mathbf{L}_k (\mathbf{z}_k - \mathbf{H}_k \bar{\mathbf{x}}_k) \quad (2)$$

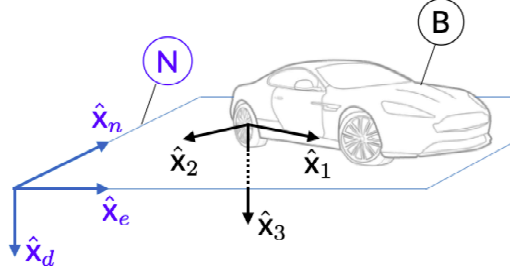


Fig. 1: Dynamic constraints acting on a ground vehicle

where \mathbf{L}_k and \mathbf{H}_k are the optimal Kalman gain and observation matrices at time epoch k .

The innovation sequence monitor utilizes Kalman filter innovation history. The innovation vector γ at time epoch k is defined as

$$\gamma_k = \mathbf{z}_k - \mathbf{H}_k \bar{\mathbf{x}}_k \quad (3)$$

A cumulative test statistic q at time epoch k is defined as the sum of squares of the normalized innovation vectors over a certain period of time as

$$q_k = \sum_{i=1}^k \gamma_i^T \mathbf{S}_i^{-1} \gamma_i \quad (4)$$

where \mathbf{S}_i is the innovation vector covariance matrix at time epoch i .

The monitor simply checks whether the test statistic q_k is smaller than a pre-defined threshold T_k^2 as

$$q_k \geq T_k^2 \quad (5)$$

Let n be the number of measurements for each GNSS measurement update; under fault free conditions, the test statistic q_k at the k^{th} GNSS measurement update is chi-square distributed with kn degrees of freedom. For a given false alarm requirement P_{FA} , the threshold T_k^2 is determined from the inverse chi-square cumulative distribution function. The innovation sequence monitor alarms for a fault if $q_k > T_k^2$. Under faulted conditions, q_k is non-centrally chi-square distributed with a non-centrality parameter λ_k^2 ,

$$\lambda_k^2 = \sum_{i=1}^k \mathbb{E}[\gamma_i]^T \mathbf{S}_i^{-1} \mathbb{E}[\gamma_i] \quad (6)$$

which is used to evaluate the probability of missed detection.

One can upperbound the integrity risk for the innovation sequence monitor at any epoch as

$$\mathbf{I}_r \leq 2Q \left\{ \frac{\ell}{\sigma^{(0)}} \right\} (1 - P_{\text{FA}}) + \sum_{i=1}^N P \left\{ |\hat{\varepsilon}_0| > \ell, q \leq \chi^{2-1} \{1 - P_{\text{FA}}, nk\} \mid \mathbf{f}_i \right\} P_{\text{H}_i} \quad (7)$$

where P_{H_i} is prior fault probability for i^{th} hypothesis, $\hat{\varepsilon}_0 \sim \mathcal{N}(\mu_0, \sigma^{(0)2})$ is the estimation error for the state of interest obtained from full-set solution, q is the test statistic i.e., sum of innovation norms, ℓ is the alert limit, and n is the number of measurements at time epoch k . \mathbf{f}_i is the worst case measurement fault vector. The bound in (7) is computed using the sequential failure mode slope (FMS) approach described in [11]. Note that the state of interest can be extracted from the full state vector as $\varepsilon = \mathbf{T}_\varepsilon \mathbf{x}$

B. Multiple Hypothesis Solution Separation Monitor

Under n single-satellite fault hypotheses, there are n solution separations

$$\Delta_i = \hat{\varepsilon}_0 - \hat{\varepsilon}_i \quad (8)$$

where $\hat{\varepsilon}_i$ is the state estimate error, obtained from subset measurements using all satellites except satellite i for $i = 1, \dots, n$.

A fault is detected if

$$\bigcup_{i=1}^n |\Delta_i| \geq T_i \quad (9)$$

where T_i is the detection threshold based on false alarm rate derived from a predefined continuity requirement to limit the false alarm rate.

An integrity risk upper bound for a MHSS monitor at any time epoch was defined in [9] as:

$$I_r \leq 2Q \left\{ \frac{\ell}{\sigma^{(0)}} \right\} + \sum_{i=1}^N Q \left\{ \frac{\ell - Q^{-1} \left\{ \frac{P_{FA}}{2N} \right\} \sqrt{\sigma^{(i)^2 - \sigma^{(0)^2}}}{\sigma^{(i)}} \right\} P_{H_i} \quad (10)$$

where ℓ is the alert limit, N is the number of hypotheses including single and multi-satellite faults, $\sigma^{(i)}$ is the standard deviation of subset solution using all measurements except the i^{th} , $\sigma^{(0)}$ is the standard deviation of the full set solution.

III. DYNAMIC CONSTRAINTS

The dynamic constraints on the ground vehicle may improve both the estimator and detector performance since they provide additional observations on velocity and attitude in body frame (Fig. 1). This improves inertial bias estimation. For example, restricted motion in the body lateral direction reduces the drift due to yaw gyroscope and lateral accelerometer biases.

One of the well-known approaches to fuse these additional observations in Kalman filters is that performing zero measurement updates in velocity- and attitude-level at INS sampling rate. This is a practical solution because it does not require any change in INS mechanization and process models, or GNSS measurement model. However, evaluating monitor performance using a Kalman filter at two different measurement update rates is cumbersome, especially when computing the worst-case fault for innovation sequence monitor. Instead, in this paper we propose a new approach that utilizes a reduced-order INS model, incorporated with both MHSS and IS monitors with minimal computation. We present derivations of the reduced-order model in Appendix A.

IV. PERFORMANCE OF MHSS VS. IS MONITORS

Using (10) and (7) with the automotive-grade IMU and DGPS settings in Table I and Table II, single satellite fault integrity performances of MHSS vs IS are compared for a tightly-coupled INS/GPS integration scheme.

TABLE I: Different Quality IMU Specifications

Parameter	AUTO	IND	LTAC	HTAC	NAV	units
Gyro Bias Stability	17.5	38	0.15	0.1	0.01	deg/hr
Angular Random Walk	0.97	0.6	0.5	0.06	0.0018	deg/ $\sqrt{\text{hr}}$
Acceleration Bias Stability	0.31	0.11	0.05	0.2	0.01	mg
Velocity Random Walk	1.04	0.076	0.07	0.0293	0.0018	m/s/ $\sqrt{\text{hr}}$

TABLE II: GPS Settings

Parameter	GPS	units
P_{FA}	10^{-6}	-
P_{H_i}	10^{-5}	-
ℓ	0.5, 1, 2, and 3	m
n_{SV}	6, 5, and 4	-

In Fig. 2, integrity risks corresponding to varying alert limits are obtained. MHSS outperforms IS especially for large alert limits. The integrity risk using the IS monitor approaches $n_{SV} \times P_{H_i} = 6 \times 10^{-5}$ because as time

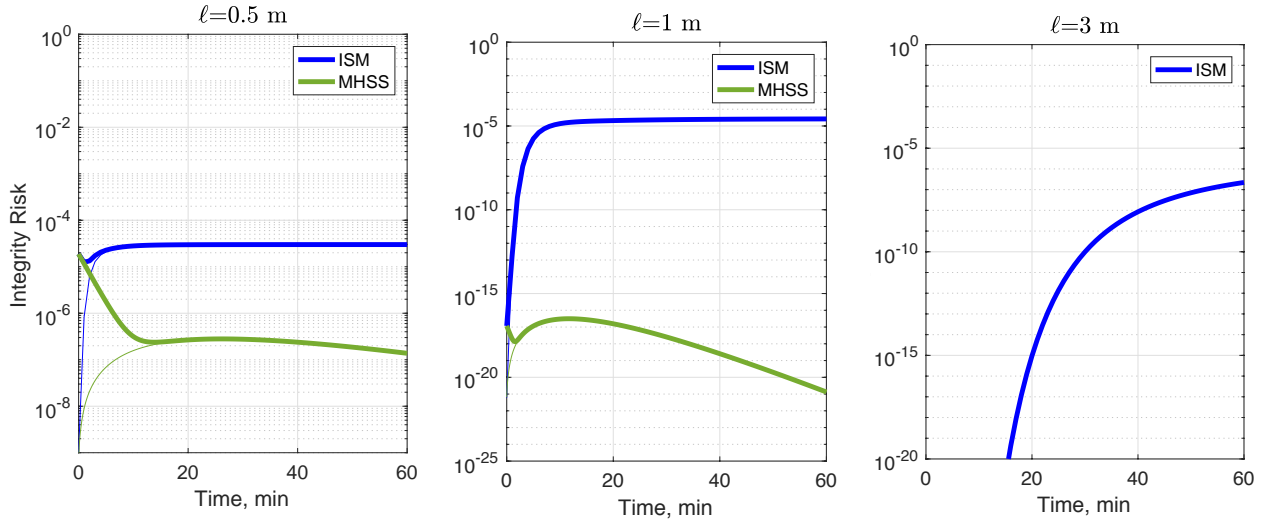


Fig. 2: The effect of horizontal alert limit on integrity risk when $n_{SV} = 6$.

progresses, the number of degrees of freedom of the IS test statistic increases causing the IS detection threshold to increase. In contrast, for MHSS, the threshold stays constant while cycle ambiguity estimation performance improves over time, enabling a lower risk. However, depending on the integrity requirement and length of operation, the IS performance may still be sufficient, and it can be used as a computationally cheaper alternative to MHSS. For example, for a relatively looser alert limit of 3 m with good satellite visibility (e.g., $n_{SV} = 6$), the integrity risk of the IS monitor remains lower than 10^{-7} for an hour, which maybe sufficient for some applications.

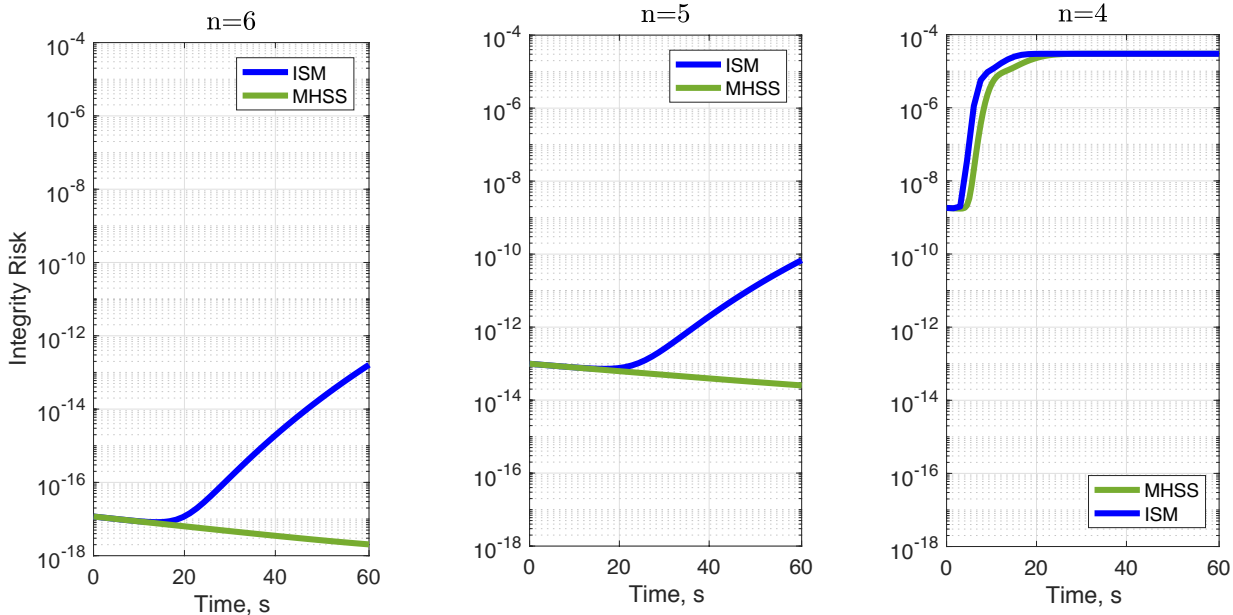


Fig. 3: The effect of number of satellites in view ($n_{SV} = 6$, $n_{SV} = 5$, and $n_{SV} = 4$ from left to right) on integrity risk when $\ell = 1$ m.

The effect of the number of satellites in view on integrity performance is evaluated in Fig. 3. Even though the MHSS outperforms the IS for strong satellite geometries ($n_{SV} \geq 5$), its performance is similar to that of IS

under poor visibility ($n_{SV} \leq 4$). This should be taken into account when designing a monitor for urban navigation application where the satellite visibility will be poor.

V. PERFORMANCE LEVERAGE FROM DYNAMIC CONSTRAINTS

The required alert limit in lateral direction for autonomous cars is very stringent (sub-meter level). The previous section suggests that MHSS may provide better integrity, thereby smaller protection levels than IS monitor does at the cost of higher computation. Therefore, this section focuses on performance of MHSS only and evaluates the minimum achievable protection levels (PL).

A. Scenario Settings

The scenarios used in simulation are selected to reflect urban canyons, where there is no satellite redundancy throughout most of the operation, i.e., where the number of satellites is equal to or lower than four, which is often the case in urban canyons. To model multipath effects, we use stochastic models obtained from GNSS data collected on a highway with overpasses and road signs. To leverage the dynamic constraints described earlier, including holonomic (no displacement perpendicular to road surface) and non-holonomic (no lateral sliding) constraints, the reduced-order INS mechanization is incorporated in the MHSS monitor.

In simulations, we assume a differential GPS representative of typical PPP accuracy. The simulation scenario is described in Fig. 4. Prior to entering an urban canyon with low sky visibility and high multipath conditions,

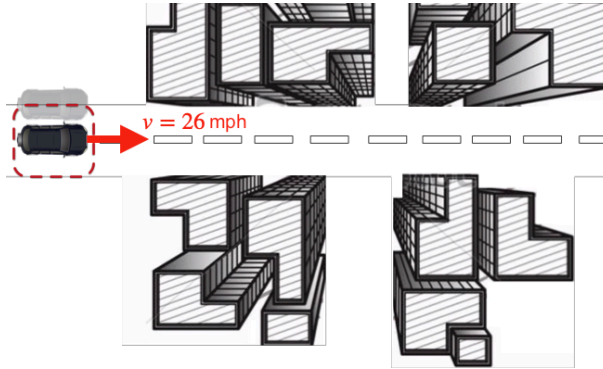


Fig. 4: A vehicle with a well initialized INS, is penetrating an urban canyon with a speed of 26 mph. The required cross-track protection level (PL) is 1m.

the INS/GPS Kalman filter is at steady state. That is, the INS error states have been initialized using GPS under good visibility ($n_{SV} \geq 6$) and low multipath. The 1σ steady-state error values for attitude (roll ϕ , pitch θ , yaw ψ), accelerometer (b_a) and gyroscope (b_g) biases are shown in Table III:

TABLE III: Steady-state errors of INS/GPS with $n_{SV} = 6$

State	AUTO	IND	LTAC	HTAC	NAV	units
ϕ	0.41	0.11	0.05	0.022	0.0011	deg
θ	0.41	0.1	0.049	0.022	0.0011	deg
b_{a_x}	0.17	0.11	0.05	0.2	0.01	milli-g
b_{a_y}	0.17	0.11	0.05	0.2	0.01	milli-g
b_{a_z}	0.156	0.046	0.034	0.048	0.0027	milli-g
b_{g_x}	0.004	0.0078	1.4×10^{-4}	2.8×10^{-5}	2.7×10^{-6}	deg/s
b_{g_y}	0.004	0.0078	1.4×10^{-4}	2.8×10^{-5}	2.7×10^{-6}	deg/s
b_{g_z}	0.005	0.01	1.4×10^{-4}	2.8×10^{-5}	2.8×10^{-6}	deg/s

With an automotive grade IMU, we assume a yaw angle ψ that is initialized to the half accuracy of pitch θ and roll ϕ angles, that is $\sigma_\psi = 0.82$ which is usually achieved using maneuvers, magnetometer-aid, or gyro-compassing techniques. In simulations, it is assumed that once the vehicle enters the urban canyon, the sky visibility and multipath

condition degrade. In the covariance analysis, for low multipath conditions, for code and carrier phase multipath and thermal noise 80 cm and 1.2 cm 1σ error values are used with a 100 s correlation time constant, respectively. For high multipath, these values are 130 cm on code and 3.3 cm on carrier phase with a shorter correlation time constant of approximately 60 s.

As in the previous section in Table II, the following values are assumed: $P_{H_i} = 10^{-5}$ for single satellite faults, and $P_{FA} = 10^{-6}$.

B. Covariance Analysis Results

Integrity risk for a geometry with satellite redundancy ($n_{SV} \geq 5$) is shown in Fig. 5. It can be seen that regardless of the quality of inertial the integrity risk levels off around similar values. This suggests that the contribution of inertial sensors are minor when there is GPS satellite redundancy. Furthermore, with the dynamic constraints, the integrity risk is smaller than 10^{-7} for $n_{SV} \geq 5$.

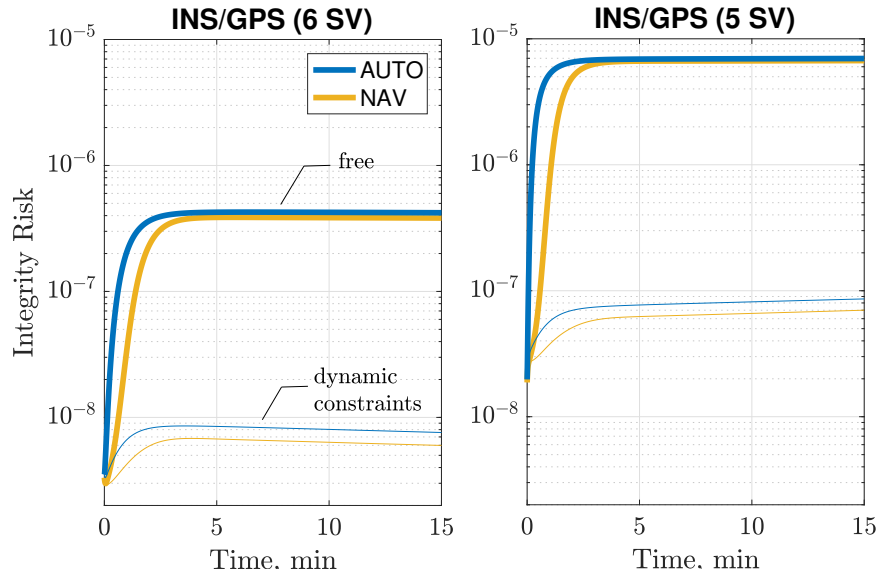


Fig. 5: MHSS Integrity risk when there is GPS redundancy: with and without ground vehicle dynamic constraints

As seen in the left hand side of Fig. 6, in the absence of measurement redundancy, that is $n_{SV} \leq 4$, using an INS and using one of high grade (navigation versus automotive) has a major impact on integrity performance. For $n_{SV} = 4$, the integrity risk without the dynamic constraints exceeds the prior fault probability 3×10^{-5} whereas for example using an automotive-grade IMU with the dynamic constraints it stays below 4×10^{-7} .

The right hand side of Fig. 6 shows the integrity risk with poor sky visibility ($n_{SV} = 3$). In this case, since there is no GPS observability, 1σ position error grows unboundedly over time and integrity risk approaches to 1; the fault-free HMI probability increases and gradually becomes the biggest contributor to integrity risk (Fig. 8). This can be seen from the figure: the integrity risk (without the dynamic constraints) reaches 1. However, with dynamic constraints, the system has sufficient observability on the position states and achieves bounding the integrity risk that approaches the prior fault probability 2×10^{-5} .

Since the integrity risk results for $n_{SV} = 3$ are unsatisfactory (i.e. larger than 10^{-7}) even with the dynamic constraints, we also investigate INS-only coasting performance to cover temporary low visibility condition during urban canyon navigation. This would eliminate the integrity risk associated with GPS fault modes. Fig. 8 shows 1σ position error and integrity risk values over time. Note that the fault-free integrity risk here is computed using an alert limit of 1 m. The alert limit is too tight to be achieved with this inertial-only configuration, for example when using a low tactical grade inertial, the integrity risk level of $I_r \leq 10^{-7}$ is guaranteed for up to 12 s.

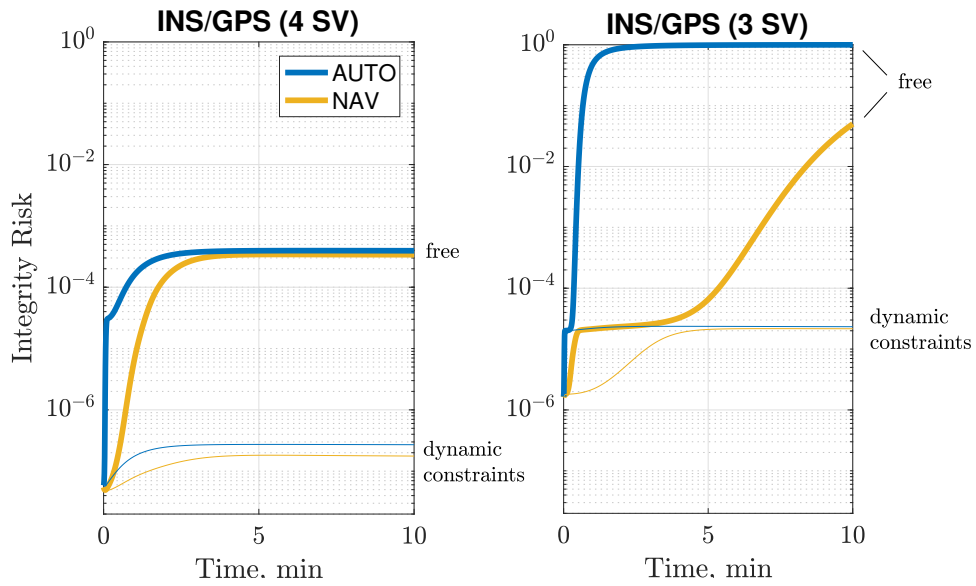


Fig. 6: MHSS Integrity risk when there is no GPS redundancy (left) and there is no GPS observability (right): with and without ground vehicle dynamic constraints

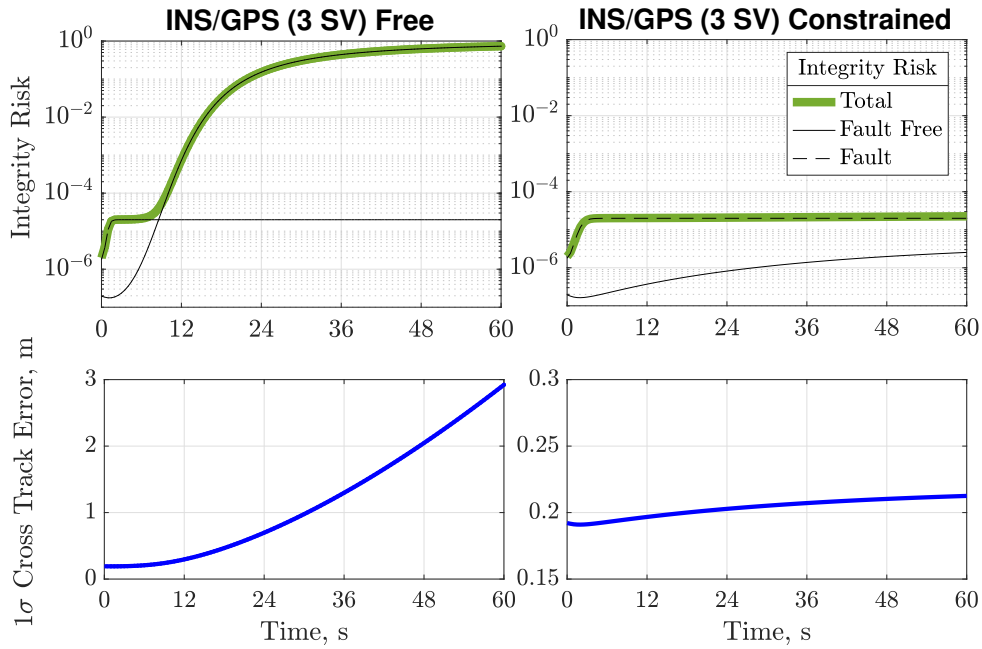


Fig. 7: Contributions of fault-free and faulty components of integrity risk

C. Protection Levels

The results so far suggest that 1m protection levels are too tight to be achieved with any configuration of INS/GPS when $n_{SV} = 3$. This section will identify the requirements and will determine the protection levels that can be realistically achieved in different sky visibilities. We performed an iterative analysis to find protection levels with different integrity risk requirements (10^{-7} , 10^{-6} , 10^{-5}), the results of which is presented in Fig. 9.

Table. 10 summarizes the simulation results. It should be noted that for cases: tightly-coupled IMU/GPS with

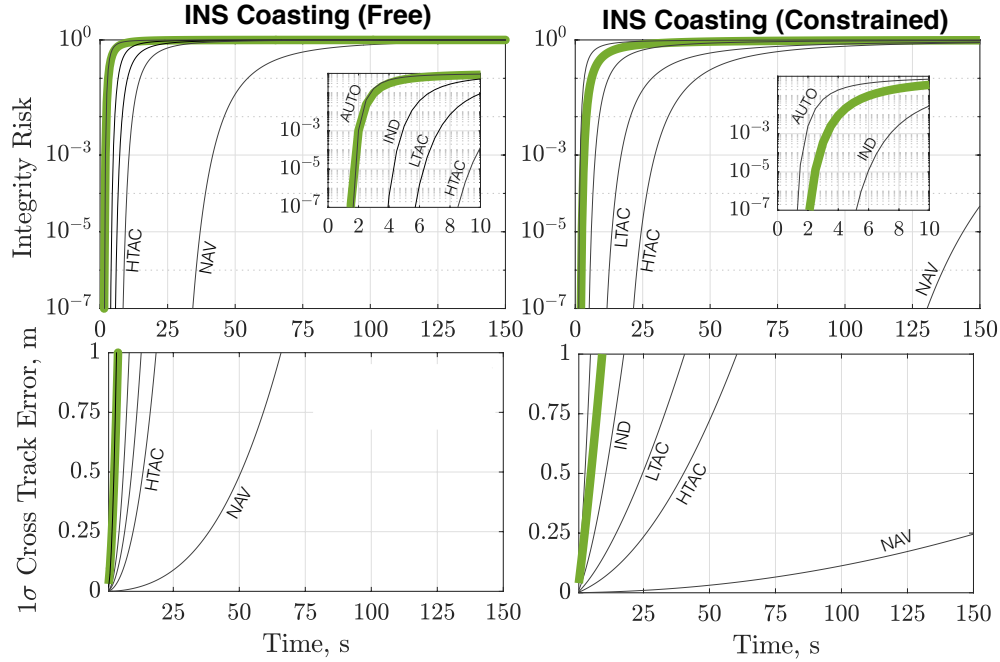


Fig. 8: Inertial coasting integrity performance with 1m protection level

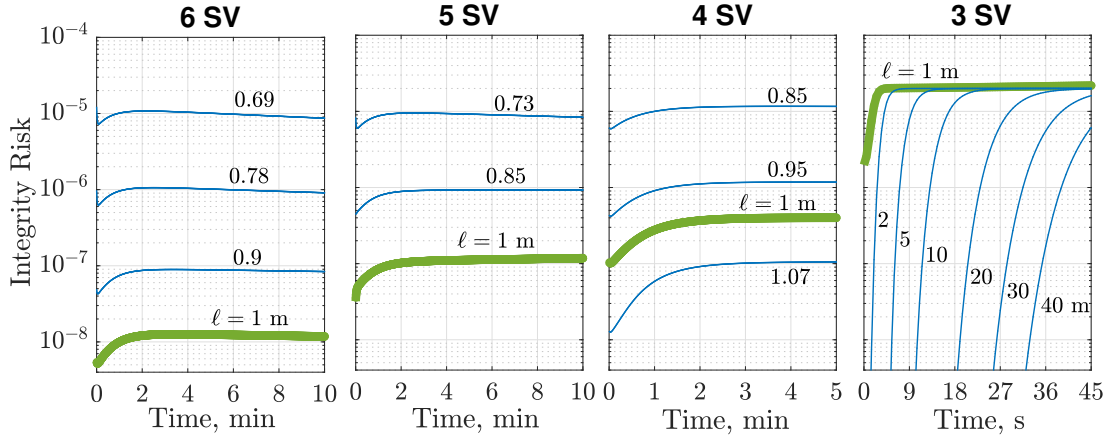


Fig. 9: Protection levels for different integrity requirements with dynamic constraints

$n_{SV} = 3$ and IMU-only, the protection levels are not bounded over time since there is not enough redundancy and observability on the position states. Therefore, the last two rows of the table show the protection levels after 30 s of low visibility condition, which is indicated by the star symbol next to the PL value.

VI. SATELLITE OUTAGE HANDLING IN MHSS USING BANK OF KALMAN FILTERS

For simplicity in the covariance analyses in previous sections, the satellite in and out cases during operation were not considered. However, urban GNSS-based navigation is impacted by frequent satellite blockages caused by buildings and other obstructions in the surrounding environment. In solution separation-based integrity monitoring, where there is one sub-filter for each satellite failure mode, satellite outages are problematic. When a satellite i goes out of sight, all subfilters will still be affected by past-time measurements from satellite i except the ones that exclude all signals over time from satellite i . These past-time measurements, if faulted, will impact the subfilter

	GPS has	Case	IR _{req}			m
			< 10 ⁻⁷	< 10 ⁻⁶	< 10 ⁻⁵	
Protection Levels	redundancy and observability	IMU + 6 SV	0.9	0.78	0.69	
		IMU + 5 SV	1	0.85	0.73	
	no redundancy	IMU + 4 SV	1.07	0.95	0.85	
	no observability	IMU + 3 SV	35 *	29 *	22 *	
	N/A	IMU Only	5.6 *	5.2 *	4.7 *	

Fig. 10: Protection levels for automotive-grade IMU with dynamic constraints. (* PL after 30 s.)

inertial bias estimates. Unless fault modes associated with satellite i are monitored indefinitely, all subfilters must be re-initialized to ensure that they are free of potential past-time faults from satellite i . The re-initialization leads to temporary poor estimates and therefore causes low detection capability until the filters converge again.

This paper addresses the above problems by introducing a new sub-filter handling approach using "fading filters" that temporarily monitor prior faults associated with previously in-sight satellites. The proposed approach eliminates INS memory loss and attenuates potential drops in detection capability of the monitor due to weakened geometry. It also minimizes the number of sub-filters.

A. Detection and Exclusion

Fig. 11 describes an MHSS filter handling structure when a fault detected and excluded for an example 3-satellite-in-view scenario. In the figure, the main filter (red) generates the navigation solution $\hat{\mathbf{x}}^{(0)}$ by using all-in-view satellite measurements, whereas the sub-filters (black) produces state estimates $\hat{\mathbf{x}}^{(i)}$ using all measurements except from the i^{th} satellite subset. The sub-filters here are used for obtaining the solution separations. When a fault is detected on a satellite, as a part of the exclusion process, the fault-free sub-filter associated with this fault mode will become the new main filter. Since the rest of the sub-filters will contain the fault, they should be re-initialized. However, in this case protection levels will be high until the restarted filters converge again. One way to address this problem is to keep additional back-up filters (blue) that use "two-out" measurement combinations. They can then replace the relevant sub-filters in the event of exclusion [9] [10].

Unlike in Fig. 11, for systems using a higher number of measurements (i.e., $n \geq 3$) and using back-up filters, some of these back-up filters will be corrupted by faulty measurement. To clear the effect of the fault, these filters should be directly re-initialized. This is the only option because due to computational limitations we only keep up to two-out sub-filter combinations. However, the re-initialization on back-up filter level does not impact the protection level unless another exclusion event occurs before the filters converge, which is very unlikely considering satellite fault statistics.

B. Sub-filter Handling for a New Satellite

When a new satellite comes in sight, its measurements can be added into each one of the filters including main, sub-, and back-up filters. In addition, a new sub-filter must branch out of the main filter which monitors the fault mode associated with the new satellite. Similarly, back-up filters for new two-out combinations are branched out from the sub-filters which in case of following satellite outages or exclusions, will rise into the sub-filter level.

In Fig. 12, satellite 4 comes in-sight into the 3-satellite bank of filters at t_1 . As seen in the figure, after t_1 the main filter labeled (0) remains the same. For the new fault mode, a new sub-filter branches out from the main filter branch without using the new satellite measurements. A similar process is applied to each one of the sub-filter branches to create the new backup filters. One can notice that the addition of a new satellite does not require filter initialization, therefore it does not cause any sudden increase in protection levels.

C. Fading Filters for Handling a Satellite Set

For clarity of exposition, let us consider a case when there are no events of FDE and new satellite coming in sight. The total number of filters n_f is a function of number of satellites n and can be expressed as:

$$n_f = C(n, 0) + C(n, 1) + C(n, 2) = \frac{n^2 + n + 2}{2} \quad (11)$$

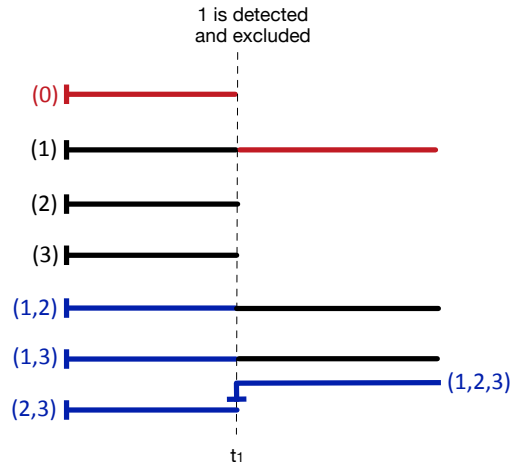


Fig. 11: MHSS fault detection and exclusion scheme. The red line stands for the main filter that utilizes all measurements. The black lines are called sub-filters using all measurement except the one in the parentheses. The red lines are called "back-up" filters which uses all measurements except the two indicated in parentheses. A fault is detected and excluded at t_1 , where some of the backup filters become subfilter, and the one that has been using the faulty satellite measurements (2,3) is re-initialized.

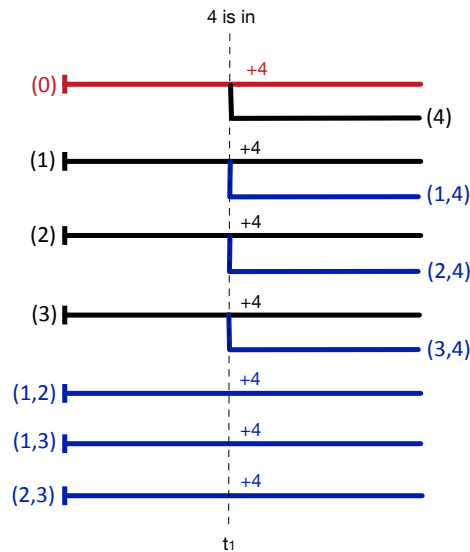


Fig. 12: MHSS new satellite handling. When satellite 4 comes in sight at t_1 , a new sub-filter labeled (4) branches out from the main filter (0). This is the one excluding measurements from satellite 4. Also, new backup filters (1,4), (2,4), and (3,4) branch out from the sub-filters (1), (2), and (3), respectively.

where C is the combination operator. Unfortunately, when a satellite sets or is blocked, sub-filter handling is much more complicated than that in FDE and the new satellite events, and Equation (11) becomes invalid. This section explains what that is and proposes an approach to minimize the number of filters used at any single time epoch while preventing potential jumps in protection levels.

When a satellite sets, all filters that have been using its measurements are corrupted if the satellite was faulted. One conservative approach to address this issue would be to apply the same filter handling as when a fault is

detected and excluded: 1) replace all subfilters with the backup filters 2) initialize new backup filters 3) immediately stop monitoring the fault mode associated with the previously in-sight satellite. As mentioned earlier this will lead temporary transient filters at the backup filter level. Unlike the exclusion event, a satellite setting is a frequent event especially when driving through areas. Therefore, in case of another immediately succeeding set (or blockage) when the backup filters need to be replaced with the sub-filters, the protection levels will drastically increase due to the unconverged filters.

Another approach would be to: 1) continue running all filters as they are, including the sub-filter for the satellite that went out of view because it was setting and 2) stop monitoring the out-of-view satellite fault mode when sufficiently long time has passed after the setting satellite (that is, when the setting satellite's effect on the filters has become negligible). Unfortunately the "sufficiently long time" does not guarantee that the filters are completely free of the effect of a potential prior fault on the setting satellite. For example in INS/GNSS, undetected prior faults might have altered the inertial bias estimates such as gyro bias, which will not manifest itself in the position level unless the vehicle maneuvers. That is, the impact of a fault on the filters is not only dependent on time but also on how the vehicle maneuvers over time.

To address these points, we propose a fading filter approach where when satellite i sets, we do the followings:

- Re-initialize backup filters that has used satellite i .
- Continue monitoring prior fault mode i until the re-initialized back up filters converge.
- Once they converge, replace the main filter with sub-filter (i), replace the rest of the subfilters with the corresponding backup filters that have never used i .

The nominal scenario for the proposed satellite outage handling is shown in Fig. 13. In the figure, at t_1 satellite 3 sets, which is followed by a fading period ($t_1 \leq t \leq t_2$) where the number of filters are one more than it was before the setting of satellite 3.

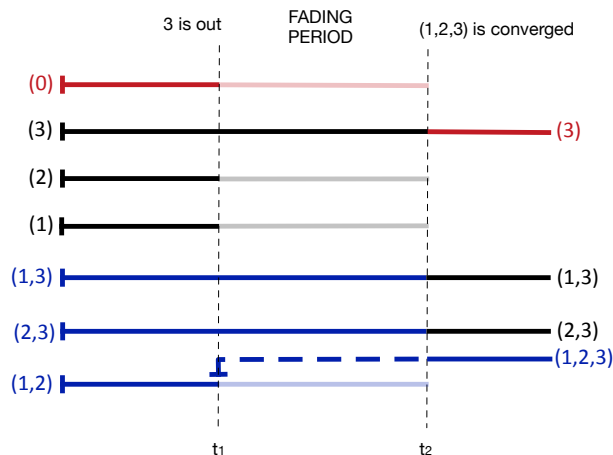


Fig. 13: Fading filter approach for a single satellite outage. Horizontal dashed lines represent transient filters whereas the solid lines indicate that the filter is at steady-state. The fading filters are shown with pale colors meaning that they will be dumped at the end of the fading period. During the fading period, under the prior fault hypothesis (3) branch (0) will be faulty and branch (3) will be fault-free, therefore it can be monitored by using solution separation $\hat{\epsilon}_3 - \hat{\epsilon}_0$. Regardless of the prior fault hypothesis, the existing fault hypotheses can be monitored by looking at their separation from the master filter.

If there is another satellite setting before the backup filter converges, instead of immediately re-initializing other back up filters, the proposed method queues the reinitialization process for each satellite set. This prevents the number of filters at any single epoch from growing unboundedly as multiple satellites set. An example queuing during the two successive satellite sets is illustrated in Fig. 14. To generalize, regardless of the frequency of the

satellite setting, the maximum number of simultaneous filters throughout an operation is bounded with the following formula:

$$n_f = C(n, 0) + C(n, 1) + C(n, 2) + C(n - 1, 2) = n^2 - n + 2 \quad (12)$$

where n is the maximum number of satellites in view at any single time epoch. Notice that the only difference between (11) and (12) are the fourth term in (12), which takes satellite outage handling into account. This additional term eliminates jumps in protection level with the cost of additional filters. However, the proposed queuing fading filter approach here minimizes the number of the additional filters and establishes a safe approach to clear the memory of the estimator (or INS) from undetected prior faults impacting previously visible satellites.

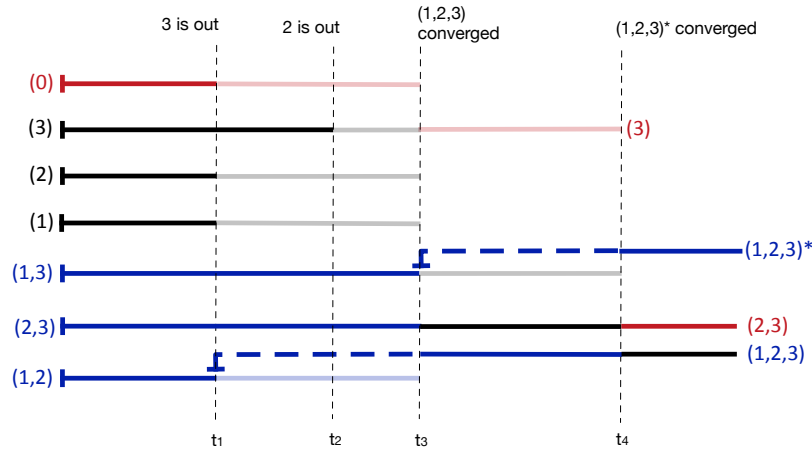


Fig. 14: Queuing in fading filter approach in the event of immediate successive satellite outages. For the simplicity, this example is only for demonstrating how re-initialization queuing over a bank of Kalman filters (starting with 3 satellites), therefore notice the filters (1,2,3) and (1,2,3)* are theoretically the same and (1,2,3)* is useless in this specific scenario; however, for larger number of satellites they will be different and both of them will be useful.

VII. CONCLUSION

The key findings of the analysis in this paper are the followings. The use of dynamic constraints with a low cost inertial sensor can provide the means to ensure tight protection levels. With aviation integrity and continuity requirements, sub-meter level protection levels are achievable using a tightly coupled INS/GNSS system when four or more satellites are visible. With three or fewer satellites, it is demonstrated that, depending on duration of the operation, INS-only coasting may provide tighter protection levels than tightly coupled INS/GNSS. In urban canyons, there are often too few GNSS signals to get a position fix using GNSS alone. In such situations, tightly coupled implementations are desirable because they make use of these few GNSS signals to limit the drift of the INS. However, the analysis results show that these few GNSS signals may not provide a significant contribution to preserving integrity (e.g., as compared to coasting using INS only). In low sky visibility condition, using a loosely coupled INS/GNSS configuration might be considered to reduce the integrity risk. It should be noted that the results obtained in the analysis are very sensitive to the prior fault and false alarm probabilities, therefore needs to be refined for other application specific requirements.

APPENDIX A
DERIVATION OF REDUCED-ORDER INS DYNAMICS

The INS kinematic model for error states is given as [13]:

$$\begin{bmatrix} \delta \dot{\mathbf{r}}^{(n)} \\ \delta \dot{\mathbf{v}}^{(n)} \\ \delta \dot{\mathbf{E}}^{(n)} \end{bmatrix} = \underbrace{\begin{bmatrix} 0 & 1 & 0 \\ 0 & -2\boldsymbol{\omega}_{ie}^{(n)} & \mathbf{N}^{\mathbf{R}^{\mathbf{B}^*}} \mathbf{f}_{\times}^{*(b)} \\ 0 & 0 & \mathbf{K}^* \end{bmatrix}}_{\mathbf{F}_n} \underbrace{\begin{bmatrix} \delta \mathbf{r}^{(n)} \\ \delta \mathbf{v}^{(n)} \\ \delta \mathbf{E}^{(n)} \end{bmatrix}}_{\mathbf{x}_n} + \underbrace{\begin{bmatrix} 0 & 0 \\ \mathbf{N}^{\mathbf{R}^{\mathbf{B}^*}} & 0 \\ 0 & \mathbf{Q}_{\mathbf{BE}}^{*-1} \end{bmatrix}}_{\mathbf{G}_u} \underbrace{\begin{bmatrix} \delta \mathbf{f}^{(b)} \\ \delta \boldsymbol{\omega}_{ib}^{(b)} \end{bmatrix}}_{\mathbf{u}} \quad (13)$$

Where,

$$\mathbf{Q}_{\mathbf{BE}} = \begin{bmatrix} 1 & 0 & -\sin(E_2) \\ 0 & -\cos(E_1) & \cos(E_2)\sin(E_1) \\ 0 & -\sin(E_1) & \cos(E_2)\cos(E_1) \end{bmatrix} \quad (14)$$

$$\mathbf{K}^* = \begin{bmatrix} \mathbf{s}^{*T} & 0 & 0 \\ 0 & \mathbf{s}^{*T} & 0 \\ 0 & 0 & \mathbf{s}^{*T} \end{bmatrix} \begin{bmatrix} \frac{\partial \mathbf{Q}_{\mathbf{BE}}^{-1}}{\partial E_1} \\ \frac{\partial \mathbf{Q}_{\mathbf{BE}}^{-1}}{\partial E_2} \\ \frac{\partial \mathbf{Q}_{\mathbf{BE}}^{-1}}{\partial E_3} \end{bmatrix}^* + \begin{bmatrix} \boldsymbol{\omega}_{ie}^{(n)T} & 0 & 0 \\ 0 & \boldsymbol{\omega}_{ie}^{(n)T} & 0 \\ 0 & 0 & \boldsymbol{\omega}_{ie}^{(n)T} \end{bmatrix} \begin{bmatrix} \frac{\partial \mathbf{R}^{\mathbf{B}^{\mathbf{N}}}}{\partial E_1} \\ \frac{\partial \mathbf{R}^{\mathbf{B}^{\mathbf{N}}}}{\partial E_2} \\ \frac{\partial \mathbf{R}^{\mathbf{B}^{\mathbf{N}}}}{\partial E_3} \end{bmatrix}^* \quad (15)$$

and \mathbf{s} is defined as,

$$\mathbf{s} = \begin{bmatrix} \boldsymbol{\omega}_{ib}^{(b)} - \mathbf{B}^{\mathbf{R}^{\mathbf{N}}} \boldsymbol{\omega}_{ie}^{(n)} \end{bmatrix} \quad (16)$$

For ground vehicles, we can assume no side-slip or vertical jump off the ground:

$$v_2^{(b)} = v_3^{(b)} = \delta v_2^{(b)} = \delta v_3^{(b)} = 0 \quad (17)$$

where $v_1^{(b)}$ and $v_2^{(b)}$ are the lateral and vertical velocity in the body frame (B).

Using the transformation matrix from navigation (N) to body (B) frame, velocity vector can be transformed as:

$$\mathbf{v}^{(b)} = \mathbf{B}^{\mathbf{R}^{\mathbf{N}}} \mathbf{v}^{(n)} \quad (18)$$

where the transformation matrix is represented in terms of Euler angles, ϕ , θ , and ψ .

Let \mathbf{B}^* be the nominal body frame, then perturbation form of the rotation matrix will be:

$$\mathbf{B}^{\mathbf{R}^{\mathbf{N}}} = \mathbf{B}^{\mathbf{R}^{\mathbf{B}^*}} \mathbf{B}^{\mathbf{R}^{\mathbf{N}}} = (\mathbf{I} + \delta \mathbf{E}_{\times}) \mathbf{B}^{\mathbf{R}^{\mathbf{N}}} \quad (19)$$

where $\delta \mathbf{E}_{\times}$ is the skew symmetric matrix of attitude deviation vector $\delta \mathbf{E} = [\delta \phi \ \delta \theta \ \delta \psi]^T$ and $\mathbf{B}^{\mathbf{R}^{\mathbf{N}}}$ is the nominal rotation matrix.

Substituting these into (18):

$$\mathbf{v}^{(b)*} + \delta \mathbf{v}^{(b)} = (\mathbf{I} + \delta \mathbf{E}_{\times}) \mathbf{B}^{\mathbf{R}^{\mathbf{N}}} (\mathbf{v}^{(n)*} + \delta \mathbf{v}^{(n)}) \quad (20)$$

Removing the nominal parts gives a linear equation as:

$$\mathbf{v}^{(b)*} + \delta \mathbf{v}^{(b)} = \mathbf{B}^{\mathbf{R}^{\mathbf{N}}} \mathbf{v}^{(n)*} + \mathbf{B}^{\mathbf{R}^{\mathbf{N}}} \delta \mathbf{v}^{(n)} + \delta \mathbf{E}_{\times} \mathbf{B}^{\mathbf{R}^{\mathbf{N}}} \mathbf{v}^{(n)*} + \delta \mathbf{E}_{\times} \mathbf{B}^{\mathbf{R}^{\mathbf{N}}} \delta \mathbf{v}^{(n)} \quad (21)$$

Taking out the nominal and second order terms gives:

$$\delta \mathbf{v}^{(b)} = \mathbf{B}^{\mathbf{R}^{\mathbf{N}}} \delta \mathbf{v}^{(n)} + \delta \mathbf{E}_{\times} \mathbf{B}^{\mathbf{R}^{\mathbf{N}}} \mathbf{v}^{(n)*} \quad (22)$$

$$= \mathbf{B}^{\mathbf{R}^{\mathbf{N}}} \delta \mathbf{v}^{(n)} - \mathbf{B}^{\mathbf{R}^{\mathbf{N}}} \mathbf{v}_{\times}^{(n)*} \delta \mathbf{E} \quad (23)$$

Extracting the second and third column of (23) and equating to zero as in (17) gives an additional measurement equation coming from the non-holonomic constraint as:

$$\mathbf{0} = (\mathbf{T}_{23} \mathbf{B}^{\mathbf{R}^{\mathbf{N}}}) \delta \mathbf{v}^{(n)} - (\mathbf{T}_{23} \mathbf{B}^{\mathbf{R}^{\mathbf{N}}} \mathbf{v}_{\times}^{(n)*}) \delta \mathbf{E} \quad (24)$$

where

$$\mathbf{T}_{23} = \begin{bmatrix} 0 & 1 & 0 \\ 0 & 0 & 1 \end{bmatrix} \quad (25)$$

A Gaussian white noise source $\zeta = [\zeta_2 \ \zeta_3]^\top$ with zero mean and variance are usually added to (24) as

$$\mathbf{0} = (\mathbf{T}_{23} \mathbf{B}^* \mathbf{R}^N) \delta \mathbf{v}^{(n)} - (\mathbf{T}_{23} \mathbf{B}^* \mathbf{R}^N \mathbf{v}_\times^{(n)*}) \delta \mathbf{E} + \zeta \quad (26)$$

where the strength of the noise can be chosen to reflect the extent of the expected constraint violations.

Eq. (26) can be used as a measurement model from virtual observation of non-holonomic constraint in Kalman Filter. However, it should be updated at the INS rate, not the GPS observation rate, which will make the sequential KF worst-case fault algorithm complex. Instead, we obtained a reduced-order INS model using the constraint.

To generalize the constraint problem, Eq. (26) can be written in terms of full state vector $\mathbf{x} \in \mathbb{R}^m$ as:

$$\mathbf{D}\mathbf{x} = \zeta \quad (27)$$

where $\mathbf{D} \in \mathbb{R}^{c \times m}$ and $\zeta \in \mathbb{R}^c$ where c is the number of constraints, for example $c = 2$ and \mathbf{D} has zero columns corresponding to states except $\delta \mathbf{v}^{(n)}$ and $\delta \mathbf{E}$ for the specific ground vehicle constraint problem.

Let INS process model be

$$\dot{\mathbf{x}} = \mathbf{F}\mathbf{x} + \mathbf{G}_u \tilde{\mathbf{u}} + \mathbf{G}_w \mathbf{w} \quad (28)$$

where $\tilde{\mathbf{u}} \in \mathbb{R}^6$ is the gyroscope and accelerometer measurements and $\mathbf{w} \in \mathbb{R}^6$ contains white and driving noise on the gyroscope and accelerometer measurements.

The nominal rotation matrix from body frame to navigation frame can be written in its matrix component form as follows:

$$\mathbf{B}^* \mathbf{R}^N = \begin{bmatrix} R_{11} & R_{12} & R_{13} \\ R_{21} & R_{22} & R_{23} \\ R_{31} & R_{32} & R_{33} \end{bmatrix} \quad (29)$$

The constraint equation (26) can be rewritten as:

$$R_{32} \delta v_3^{(n)} + R_{22} \delta v_2^{(n)} + R_{12} \delta v_1^{(n)} - \delta E_1 v_3^{(b)*} + \delta E_3 v_1^{(b)*} = \zeta_2 \quad (30)$$

$$R_{33} \delta v_3^{(n)} + R_{23} \delta v_2^{(n)} + R_{13} \delta v_1^{(n)} - \delta E_2 v_1^{(b)*} + \delta E_2 v_2^{(b)*} = \zeta_3 \quad (31)$$

Solving the two constraint equations for $\delta v_2^{(n)}$ and $\delta v_3^{(n)}$ gives:

$$\delta v_2^{(n)} = \frac{-R_{32} \zeta_3 + R_{33} \zeta_2 - R_{12} R_{33} \delta v_1^{(n)} + R_{13} R_{32} \delta v_1^{(n)} - R_{32} \delta E_2 v_1^{(b)*}}{D_1} + \frac{R_{32} \delta E_1 v_2^{(b)*} + R_{33} \delta E_1 v_3^{(b)*} - R_{33} \delta E_3 v_1^{(b)*}}{D_1} \quad (32)$$

$$\delta v_3^{(n)} = \frac{R_{22} \zeta_3 - R_{23} \zeta_2 + R_{12} R_{23} \delta v_1^{(n)} - R_{13} R_{22} \delta v_1^{(n)} + R_{22} \delta E_2 v_1^{(b)*}}{D_1} + \frac{-R_{22} \delta E_1 v_2^{(b)*} - R_{23} \delta E_1 v_3^{(b)*} + R_{23} \delta E_3 v_1^{(b)*}}{D_1} \quad (33)$$

Where,

$$D_1 = R_{22} R_{33} - R_{23} R_{32} \quad (34)$$

Re-writing elements of matrix \mathbf{F}_n from equation (11) in their component form we get,

$$\boldsymbol{\omega}_{ie}^{(n)} = \begin{bmatrix} \omega_{ie_1}^{(n)} \\ \omega_{ie_2}^{(n)} \\ \omega_{ie_3}^{(n)} \end{bmatrix} \quad (35)$$

$$\mathbf{f}^{*(b)} = \begin{bmatrix} \mathbf{f}_1^{*(b)} \\ \mathbf{f}_2^{*(b)} \\ \mathbf{f}_3^{*(b)} \end{bmatrix} \quad (36)$$

Using coefficients of states from equations (30) and (31) which would account for the effect of applied constraint, and removing the rows in \mathbf{F}_n , \mathbf{G}_u , \mathbf{G}_w and \mathbf{w} corresponding to $\delta v_2^{(n)}$ and $\delta v_3^{(n)}$, the reduced order kinematic model becomes

$$\begin{bmatrix} \delta \dot{\mathbf{r}}^{(n)} \\ \delta v_1^{(n)} \\ \delta \dot{\mathbf{E}}^{(n)} \end{bmatrix} = \underbrace{\begin{bmatrix} \mathbf{0} & \mathbf{F}_{12} & \mathbf{F}_{13} \\ \mathbf{0} & \mathbf{F}_{22} & \mathbf{F}_{23} \\ \mathbf{0} & \mathbf{0} & \mathbf{K}^* \end{bmatrix}}_{\mathbf{F}_{n_r}} \underbrace{\begin{bmatrix} \delta \mathbf{r}^{(n)} \\ \delta v_1^{(n)} \\ \delta \mathbf{E}^{(n)} \end{bmatrix}}_{\mathbf{x}_{n_r}} + \underbrace{\begin{bmatrix} \mathbf{0} & \mathbf{0} \\ \mathbf{G}_{u_{21}} & \mathbf{0} \\ \mathbf{0} & \mathbf{Q}_{BE}^{*-1} \end{bmatrix}}_{\mathbf{G}_{u_r}} \underbrace{\begin{bmatrix} \delta \mathbf{f}^{(b)} \\ \delta \boldsymbol{\omega}_{ib}^{(b)} \end{bmatrix}}_{\mathbf{u}} \quad (37)$$

Where,

$$\mathbf{F}_{12} = \begin{bmatrix} 1 \\ \frac{R_{13} R_{32} - R_{12} R_{33}}{D_1} \\ \frac{R_{12} R_{23} - R_{13} R_{22}}{D_1} \end{bmatrix} \quad (38)$$

$$\mathbf{F}_{13} = \begin{bmatrix} 0 & 0 & 0 \\ -\frac{R_{33} v_1^{(b)*}}{D_1} & 0 & 0 \\ \frac{R_{23} v_1^{(b)*}}{D_1} & 0 & 0 \end{bmatrix} \quad (39)$$

$$\mathbf{F}_{22} = -\frac{2\omega_{ie2}^{(n)}(R_{12}R_{23} - R_{13}R_{22}) + 2\omega_{ie3}^{(n)}(R_{12}R_{33} - R_{13}R_{32})}{D_1} \quad (40)$$

$$\mathbf{F}_{23} = \left[R_{12} \mathbf{f}_3^{*(b)} - R_{13} \mathbf{f}_2^{*(b)} - \frac{2R_{33}\omega_{ie3}^{(n)}v_1^{(b)*} + 2R_{23}\omega_{ie2}^{(n)}v_1^{(b)*}}{D_1} \quad R_{13} \mathbf{f}_1^{*(b)} - R_{11} \mathbf{f}_3^{*(b)} \quad R_{11} \mathbf{f}_2^{*(b)} - R_{12} \mathbf{f}_1^{*(b)} \right] \quad (41)$$

$$\mathbf{G}_{u_{21}} = [R_{11} \quad R_{21} \quad R_{31}] \quad (42)$$

and

$$\mathbf{G}_{w_r} = -\mathbf{G}_{u_r} \quad (43)$$

The two states of velocity errors in which directions constraint is applied, are removed from the error state kinematic model, thus reducing the model. The process noise model is additionally augmented to account for the addition of constraint process noise ζ . Thus process noise model from equation (47) becomes \mathbf{G}_{w_a} . Where,

$$\mathbf{G}_{w_a} = [\mathbf{G}_{w_r} \quad \mathbf{G}_\zeta] \quad (44)$$

$$\mathbf{G}_\zeta = \begin{bmatrix} 0 & 0 \\ \frac{R_{33}}{D_1} & -\frac{R_{32}}{D_1} \\ -\frac{R_{23}}{D_1} & \frac{R_{22}}{D_1} \\ \frac{2(R_{23}\omega_{ie2}^{(n)} + R_{33}\omega_{ie3}^{(n)})}{D_1} & -\frac{2(R_{22}\omega_{ie2}^{(n)} + R_{32}\omega_{ie3}^{(n)})}{D_1} \\ 0 & 0 \\ 0 & 0 \\ 0 & 0 \end{bmatrix} \quad (45)$$

and

$$\mathbf{w}_a = \begin{bmatrix} \mathbf{w} \\ \zeta \end{bmatrix} \quad (46)$$

Thus the INS process model reduces to

$$\dot{\mathbf{x}}_r = \mathbf{F}_{n_r} \mathbf{x}_r + \mathbf{G}_{u_r} \tilde{\mathbf{u}} + \mathbf{G}_{w_a} \mathbf{w}_a \quad (47)$$

DISCLAIMER

The opinions expressed in this paper are those of authors, and do not represent those of any other organization including Amazon Prime Air and Hexagon Positioning Intelligence.

REFERENCES

- [1] U.S. Department of Transportation, "Preparing for the Future of Transportation: Automated Vehicle 3.0," in *Technical Document*, Washington, DC, 2018.
- [2] M. Joerger, F.-C. Chan, and B. Pervan, "Towards Navigation Safety for Autonomous Cars," *Inside GNSS*, 2018.
- [3] K. Gunning, et. al., "Design and Evaluation of Integrity Algorithms for PPP in Kinematic Applications," in *Proc. ION GNSS+*, Miami, FL, 2018.
- [4] N. Zui, et. al., "GNSS Position Integrity in Urban Environments: A Review of Literature," *IEEE Transactions on Intelligent Transportation Systems*, vol. 19, no. 9, pp. 2762–2778, 2018.
- [5] C. Tanil, S. Khanafseh, M. Joerger, B. Pervan, "An INS Monitor to Detect GNSS Spoofers Capable of Tracking Aircraft Position," *IEEE Transactions on Aerospace and Electronics*, vol. 54, no. 1, pp. 131–143, Feb 2018.
- [6] N. R. Velaga, et. al., "Map- aided integrity monitoring of a land vehicle navigation system," *IEEE Trans. Aerosp. Electron. Syst.*, vol. 13, no. 2, pp. 848–858, Jun 2012.
- [7] G. Castaldo, et. al., "P-RANSAC: An integrity monitoring approach for GNSS signal degraded scenario," *Int. J. Navigat. Observat.*, vol. 2014, no. 173818, Sep 2014.?
- [8] M. Brenner, "Integrated GPS/Inertial Fault Detection Availability," *NAVIGATION, Journal of The Institute of Navigation*, vol. 43, no. 2, pp. 111–130, 1996.
- [9] J. Blanch, T. Walter, P. Enge, "Fixed Subset Selection to Reduce Advanced RAIM Complexity," in *Proc. ION ITM*, Reston, VA, 2018.
- [10] J. Blanch, K. Gunning, T. Walter, L. D. Groot, "Reducing Computational Load in Solution Separation for Kalman Filters and an Application to PPP Integrity," in *Proc. ION ITM*, Reston, VA, 2019.
- [11] C. Tanil, S. Khanafseh, M. Joerger, B. Pervan, "Sequential Integrity Monitoring for Kalman Filter Innovations-based Detectors," in *Proc. ION GNSS+*, Miami, FL, 2018.
- [12] S. Khanafseh, et. al., "GNSS Multipath Error Modeling for Automotive Applications," in *Proc. ION GNSS+*, Miami, FL, 2018.
- [13] C. Tanil, S. Khanafseh, B. Pervan, "Detecting GNSS Spoofing Attacks Using Inertial Sensing of Aircraft Disturbance Response," *AIAA Journal of Guidance, Control, and Dynamics*, vol. 40, no. 8, pp. 2006–2016, 2017.